ChemPubSoc Europe
DOI: 10.1002/cssc.201802440
CHEMSUSCHEM
Full Papers

Defect-Type-Dependent Near-Infrared-Driven Photocatalytic Bacterial Inactivation by Defective Bi_2S_3 nanorods

Hongli Sun+,[a] Zhifeng Jiang+,[a] Dan Wu,[c] Liqun Ye,[d] Tianqi Wang,[a] Bo Wang,[a] Taicheng An,*[b] and Po Keung Wong*[a, b]

Defect engineering is crucial in tailoring photocatalytic efficiency, but it suffers from uncertainty in determining the vacancy type and in which type of the vacancy can better promote the photocatalytic efficiency. In this study, Bi_2S_3 nanorods with bismuth or sulfur vacancies were synthesized to investigate their distinct effects on the electronic structure, electron–hole separation characteristics, and near-infrared (NIR)-driven photocatalytic bacterial inactivation activity. Both bismuth and sulfur vacancies can enhance the light absorption ability of Bi_2S_3. However, the lifetime of photoinduced electrons is extended by bismuth vacancies but shortened by sulfur vacancies. Owing to these tendencies, Bi_2S_3 with Bi vacancies fully inactivated 7 log *E. coli* cells within 40 min of NIR irradiation, displaying better NIR-driven photocatalytic bacterial inactivation efficiency than Bi_2S_3 with S vacancies. This study discloses the defect-type-dependent photocatalytic behaviors, providing new insights into designing highly efficient photocatalysts.

Introduction

In studies of photo- and electrocatalysis during the last few decades, vacancy engineering has been a quite powerful strategy to tailor the photo- or electrocatalytic efficiency.[1–6] It has been widely accepted that the introduction of vacancies induces the formation of new energy levels, which can narrow the band gap of the catalysts and thus enhance their light-harvesting ability. For example, the introduction of oxygen vacancies significantly improves the visible-light response in TiO_2,[7,8] $BiPO_4$,[9] Bi_5O_7Br,[10] BiOBr,[11] BiOCl,[12] BiO_{2-x},[13] and ZnO photocatalysts.[14] In addition, the introduced vacancies can modify the charge-transfer kinetics for efficient charge separation. Many studies have compared the lifetime of photogenerated electrons from the catalysts with and without vacancies, demonstrating that the vacancies are beneficial to prolong the lifetime of photogenerated electrons.[10,11] Li et al. evaluated the average lifetime of photogenerated electrons from BiOBr with and without oxygen vacancies by time-resolved photoluminescence spectroscopy and reported that the average lifetime of the photogenerated electrons in BiOBr with oxygen vacancy was more than two times that of BiOBr without oxygen vacancy. They also revealed that the oxygen vacancies in BiOBr induced some trapping sites as initial electron acceptors, which significantly increased the lifetime of the photogenerated electrons.[11] Although the vacancies are of great importance to the photocatalytic activities, some vacancy-related issues are still ambiguous and require further study. Firstly, many studies based on electron spin resonance (ESR) only serve to determine the presence of oxygen vacancies. However, the ESR signals can only prove the presence of unpaired electrons, which can be formed by a deficiency of any element of a specific catalyst. Thus, methods used to determine the type of vacancy should be more diversified and precise. Secondly, as for binary or ternary catalysts, the vacancy can be formed by a deficiency of any element, leading to catalysts with different types of elemental vacancy. However, it is not known whether all types of elemental vacancy can promote the photocatalytic efficiency. In fact, there is no solid evidence to show what kind of elemental vacancy is good for the photocatalytic efficiency. Therefore, it is necessary to synthesize catalysts with different types of elemental vacancy and to study their distinct effects on the photogenerated electron–hole separation and the photocatalytic activity for precise elaboration of the effects of elemental vacancies on photocatalytic activity.

Moreover, given the increasing severe energy shortage, utilization of the renewable energy, solar energy, as efficiently as possible in photocatalytic applications occupies the top priori-

---

[a] H. L. Sun,+ Dr. Z. F. Jiang,+ Dr. T. Q. Wang, Dr. B. Wang, Prof. P. K. Wong
School of Life Sciences, The Chinese University of Hong Kong
Shatin, NT, Hong Kong SAR (P.R. China)
E-mail: pkwong@cuhk.edu.hk

[b] Prof. T. C. An, Prof. P. K. Wong
Institute of Public Health and Environmental Pollution Control
School of Environmental Science and Engineering
Guangdong University of Technology, Guangzhou (P.R. China)
E-mail: antc99@gdut.edu.cn

[c] Dr. D. Wu
College of Materials Science and Engineering, Shenzhen University
Shenzhen, 518000 (P.R. China)

[d] Dr. L. Q. Ye
Engineering Technology Research Center of Henan Province for Solar Catalysis, College of Chemistry and Pharmaceutical Engineering
Nanyang Normal University, Nanyang (P.R. China)

[+] These authors contributed equally to this work.

Supporting Information and the ORCID identification number(s) for the author(s) of this article can be found under: https://doi.org/10.1002/cssc.201802440.

© 2019 Wiley-VCH Verlag GmbH & Co. KGaA, Weinheim

ty. To date, the light response range of most reported photocatalysts are extended to visible light only, which only occupies about 45% of the solar spectrum. As near-infrared (NIR) light constitutes about 50% of the solar spectrum, more and more efforts have been devoted to identifying NIR-responsive photocatalysts in recent years.[15–19] For instance, Li et al. explored a metal–organic framework composite, which has efficient photocatalytic hydrogen production ability owing to its broader spectral responsivity (from UV to NIR).[15] Yang et al. constructed carbonitride structures that can reduce CO_2 even under red light irradiation.[18] However, as a promising approach to address energy shortage issues, studies on the synthesis and characterization of NIR-driven photocatalysts are still limited. Therefore, it is highly desirable to develop photocatalysts with broader solar spectral response (e.g., UV to NIR region) to fully utilize the energy of sunlight.

Results and Discussion

Herein, a range of NIR-responsive Bi_2S_3 nanorods with different types of elemental vacancies were synthesized by varying the solvothermal treatment time (1 h: BS-1; 3 h: BS-3; 5 h: BS-5), to provide a platform to study their distinct effects on electronic structure, electron–hole separation, and photocatalytic activity. XRD patterns (Figure 1 a) indicates the high crystallinity of these prepared Bi_2S_3 (JCPDS No. 17-0320) nanorods with a diameter of about 20 nm (Figure 1 b). As for BS-3, clearly resolved and well-defined lattice fringes can be observed from the representative HRTEM image (Figure 1 c). The adjacent lattice distances of 0.2 and 0.194 nm are equivalent to the (002) and (501) atomic planes of Bi_2S_3, further demonstrating the good crystallinity. EDX elemental mapping images (Figure 1 d) not only confirm the coexistence of Bi and S, but also indicate the homogeneous dispersion of the two elements within the nanorods.

By comparison of the XRD patterns and SEM images of BS-1, BS-3, and BS-5, it can be discerned that the different durations of solvothermal treatment did not change the morphology or the crystal phase of Bi_2S_3. However, from the obtained ESR spectra (Figure 2), BS-1, BS-3, and BS-5 samples show different intensities of ESR signals ($g \approx 1.994$) regardless of the absence

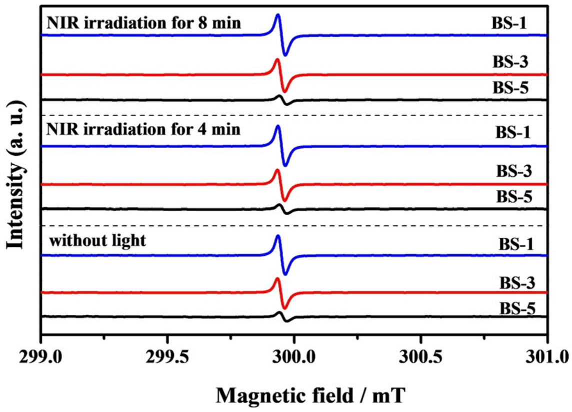

Figure 2. ESR spectra of various as-prepared Bi_2S_3 with and without NIR irradiation.

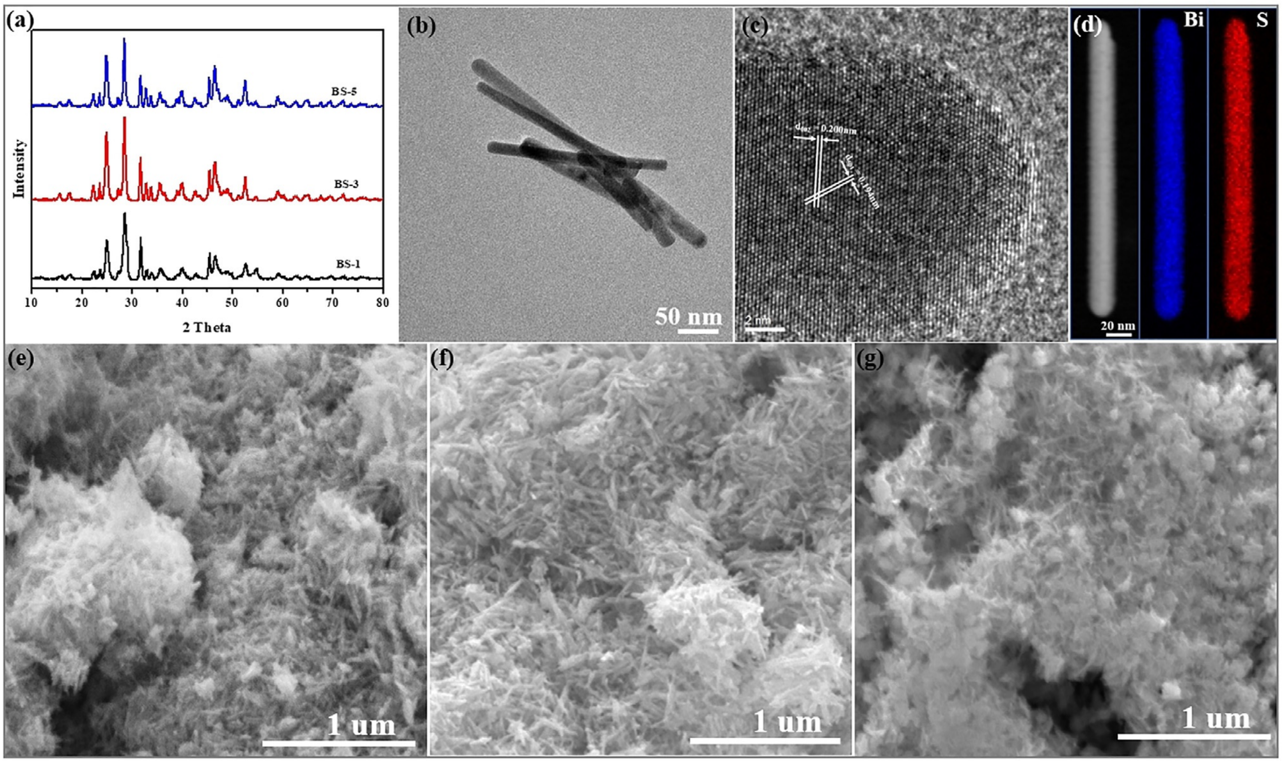

Figure 1. a) XRD patterns of the as-prepared bismuth sulfide. b) TEM, c) HRTEM, and d) elemental mapping images of BS-3. e–g) SEM images of BS-1 (e), BS-3 (f), and BS-5 (g).

or presence of NIR irradiation. These results imply that they vary from each other in the amounts of defects, owing to the different solvothermal treatment durations. As ESR tests can only prove the presence of defects caused by unpaired electrons, it cannot determine the type of vacancy. Thus, X-ray photoelectron spectroscopy (XPS) was applied to investigate the atomic ratios of these three samples to find out their vacancy type. XPS was used to determine the Bi/S ratio mainly because the effect of surface defects on photocatalysis outweighs that of bulk defects, as the bulk defects would serve as trapping sites for the charges, hindering their further migration to the surface active sites for interface reactions, whereas surface defects would be gathering center of active charges when electrons are trapped there, promoting the interface reactions. For example, Kong et al. tuned the relative concentration ratio of bulk defects to surface defects in TiO_2 nanocrystals, which efficiently promoted the photocatalytic efficiency.[3] XPS can be employed as a characterization technique to investigate the surface (up to a depth of 3 nm) chemical components and states of the materials.[1,4,20,21] Based on this, it would be suitable to explore Bi/S ratios obtained from XPS to evaluate the effects of surface defects. The Bi/S atomic ratios of the three samples differed greatly based on the XPS analysis (Table 1), suggesting BS-1 is sulfur-deficient Bi_2S_3 and BS-3 is bismuth-deficient Bi_2S_3, whereas the Bi/S atomic ratio of BS-5 is close to the theoretical value (i.e., Bi_2S_3), suggesting no or relatively little element vacancy. Moreover, the surface valence states of both bismuth and sulfur showed shifts in the binding energies (see the Supporting Information, Figure S2), which could be attributed to variations in the chemical environment caused by sulfur or bismuth vacancies. With combination of these two techniques, we can find that a deficiency of either bismuth or sulfur atoms will enhance the densities of the unpaired electrons and thus increase the amount of defects.

Table 1. Bi/S and Bi_{red}/Bi^{3+} ratios of different Bi_2S_3 samples.

Sample	Bi/S	Bi_{red}/Bi^{3+}
BS-1	0.72	1.17
BS-3	0.59	2.71
BS-5	0.67	1.05

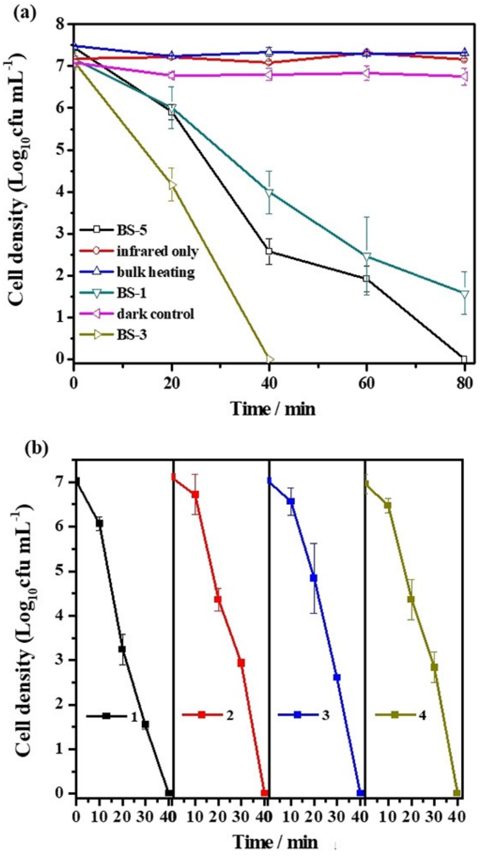

Figure 3. NIR-driven photocatalytic inactivation efficiency toward *E. coli* (10^7 cfu mL^{-1}, 50 mL) in the presence of various defective Bi_2S_3 samples (a) and BS-3 (b) for 4 cycles.

The Bi_2S_3 samples with different types of element vacancies were then used to investigate the defects' structure–activity relationship by determining their performance in photocatalytic inactivation of *E. coli* (10^7 cfu mL^{-1}, 50 mL) under NIR irradiation (Figure 3a). The population of the bacterium in the control experiments (dark control with catalyst only and light control with NIR irradiation only) remained almost unchanged after 80 min of treatment, indicating no severe inactivation effect of the as-prepared Bi_2S_3 towards *E. coli* cells and no obvious photolysis effect under NIR irradiation. However, with the combination of NIR irradiation and the various catalysts, BS-3 in particular exhibited remarkably high photocatalytic activity and could completely inactivate approximately 7 log *E. coli* bacterial cells with only 40 min of NIR irradiation. The inactivation efficiency of BS-3 was faster than that of sulfur-deficient BS-1 and BS-5. Considering the thermal effect, the temperature variations during the NIR-driven photocatalytic inactivation process were monitored, which increased up to 41 °C after 2 h of NIR irradiation (Figure S1). As a result, the inactivation efficiency towards 7 log *E. coli* by bulk heating at only 41 °C was studied for comparison. It turned out that bulk heating at 41 °C for 80 min was not strong enough to inactivate the *E. coli* cells, further demonstrating the prominent photocatalytic efficiency of the as-prepared bismuth-deficient Bi_2S_3.The SEM images of *E. coli* cells with and without treatment by Bi_2S_3 nanorods are shown in Figure S3. The initial untreated bacteria exhibited almost intact rod-shaped morphology and a well-preserved full body. However, after photocatalytic inactivation, the initial well-preserved full body collapsed severely and broken apertures could be observed. These results suggest that the Bi_2S_3 nanorods caused severe damage to the bacteria and exhibited considerable photocatalytic bacterial inactivation activity. To investigate the photostability of the bismuth-deficient Bi_2S_3, the NIR-driven photocatalytic bacterial inactivation process was repeated for four cycles (Figure 3b). BS-3 was found to retain its photocatalytic inactivation efficiency after four cycles, implying that bismuth-deficient Bi_2S_3 was quite stable under the reaction conditions.

© 2019 Wiley-VCH Verlag GmbH & Co. KGaA, Weinheim

To find out why Bi_2S_3 with different vacancy types exhibited different performances in the photocatalytic inactivation of *E. coli*, the surface areas, light absorptivities, charge abundances, charge transductions, and charge-separation abilities of these three samples were compared in detail. The surface areas of Bi_2S_3 decreased with longer solvothermal treatment time (Table S1). Although the surface area of BS-3 was not the largest, it had the best photocatalytic inactivation activity, whereas the surface area of BS-1 was the highest among the samples, but its photocatalytic efficiency was the poorest. Therefore, we suspect that the surface area was not the key factor in determining the inactivation efficiency. The spectral response ranges of all three BS samples were quite wide and extended to NIR range (Figure 4a). The onset of optical absorption was around 1000 nm, suggesting their impressive light-absorption abilities. Compared with BS-5, which had fewer vacancies, the onset of optical absorption for both BS-1 and BS-3 redshifted to higher wavelengths, indicating that the vacancies promote light absorption in Bi_2S_3 to some extent, regardless of the type of vacancy. Moreover, the band-gap energies were estimated accordingly, by using Tauc's equation, to be 1.45, 1.62, and 1.72 eV for BS-3, BS-1, and BS-5, respectively. BS-1 and BS-3 exhibited narrower band gaps, possibly because the vacancy-induced state narrowed the band gap.[12] To gain a better understanding of the variations between them, the valence band maximum (VBM) and conduction band minimum (CBM) positions were calculated based on the analysis from valence band XPS (Figure 4b) and Mott–Schottky curves (Figure 4c). The corresponding band structures are shown in Figure 4d. Compared with BS-5, it is easier for bismuth-deficient BS-3, with a narrower band gap, to be excited by NIR. Although there was no longer the advantage of higher conduction band potentials for BS-3, the CBM of BS-3 (−0.76 V) and the required overpotential were still thermodynamically favorable for the production of O_2^{-}.[22,23] However, the CBM of sulfur-deficient BS-1 was lowered to −0.33 V, at which value the overpotential needed to transform O_2 into O_2^{-} can almost be neglected. In addition, the densities of charge carriers were estimated based on the characteristics of the Mott–Schottky curve [Equation (1), taken from ref. [4]]:

$$N_\mathrm{d} = 2/(e_0\,\varepsilon\,\varepsilon_0)[\mathrm{d}(1/C^2)/\mathrm{d}V]^{-1} \qquad (1)$$

Where N_d is the carrier density of the sample, e_0 is the electron charge (1.6×10^{-19} C), ε is the dielectric constant of the sample, ε_0 is the electrical permittivity of a vacuum (8.86×10^{-12} F m^{-1}), C is the specific capacity, and V is the applied bias at the electrode. Given that all three samples are pure Bi_2S_3, the charge densities of BS-1, BS-3, and BS-5 can be compared by comparing the slopes of the linear range of the Mott–Schottky curve. The slope of BS-3 was less than that of BS-1 (Figure 4c), revealing that bismuth-deficient Bi_2S_3 had a greater charge density than sulfur-deficient Bi_2S_3. Possibly the higher electronegativity of sulfur (2.58) compared to bismuth (2.02) could cause the variations in charge density. Furthermore, the surface valence state of bismuth was investigated in detail (Figure S2). Apart from the characteristic peak at 161.2 eV, corresponding to S 2p orbitals, another four peaks are deconvoluted for Bi 4f spectra. The peaks at 164.6 and 159.3 eV are ascribed to Bi 4$f_{5/2}$ and Bi 4$f_{7/2}$ of Bi^{3+}, whereas those at 163.6

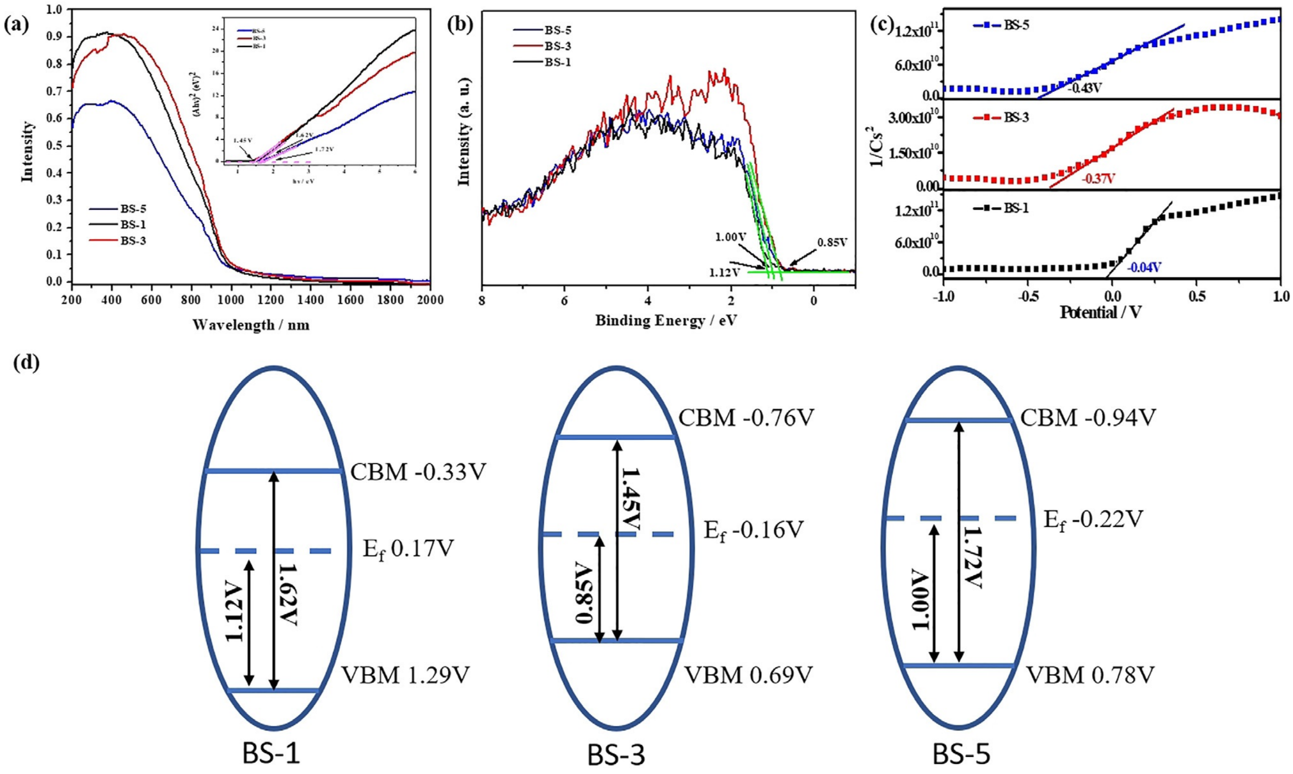

Figure 4. a) UV/Vis diffuse reflectance spectra, b) valence band XPS spectra, c) Mott–Schottky curves, and d) band structures for various Bi_2S_3 samples.

© 2019 Wiley-VCH Verlag GmbH & Co. KGaA, Weinheim

and 158.3 eV are ascribed to Bi 4$f_{5/2}$ and Bi 4$f_{7/2}$ of the partially reduced Bi.[11] The partially reduced Bi (Bi_{red}) possibly results from the reducing ability of ethylene glycol, which is used as the solvent in solvothermal treatment process. It is worth noting that the Bi_{red}/Bi^{3+} ratio of BS-3 is roughly twice those of BS-1 and BS-5, implying the higher abundance of electrons for BS-3 (Table 1). This phenomenon is consistent with the analysis of Mott–Schottky curves. Based on the above analysis, we speculate that, Bi_2S_3 with defects caused by bismuth vacancies is more likely to have higher charge densities than those with sulfur vacancies.

The photocurrent responses of BS-3, BS-1, and BS-5 were measured under NIR irradiation (Figure 5 a). The highest photocurrent of BS-3 suggests the most efficient charge photogeneration and the greatest possibility of good catalytic activity.[1] Compared with BS-5, the photocurrent of BS-3 is significantly increased, whereas that of BS-1 is dramatically decreased, even though BS-1 has higher light absorption ability than BS-5. These results indicate that the enhancement of photocurrent is not only due to the enhanced light absorption, but also highly related to the vacancy type, where bismuth vacancy-related defects promote the generation of efficient photoinduced electrons. As photogenerated electrons can recombine with holes, their involvement in the photocatalytic reaction could be hindered. The charge transportation and separation of the photogenerated charges were further studied by time-resolved transient and steady-state photoluminescence (PL) spectroscopy. For the average lifetime resolved from the transient PL spectra (Figure 5 b), BS-3 was found to have a higher average lifetime (1125.3 ps) than BS-5 (776.1 ps), whereas the average lifetime of BS-1 was shortened (638.3 ps), showing that the charges of bismuth-deficient Bi_2S_3 were transferred more efficiently with a greatly suppressed recombination rate, whereas the photogenerated electrons in sulfur-deficient Bi_2S_3 are more likely to recombine with the photogenerated holes. This is possibly because the photogenerated electrons trapped by bismuth vacancies have a slower rate of decay by recombining with holes, leading to a longer average lifetime.[10,24–26] The enhanced separation efficiency of BS-3 is further confirmed by its steady-state PL spectrum, in which the intensity is much weaker than in those for BS-1 and BS-5 (Figure 5 c), verifying the better performance of bismuth-deficient BS-3 in separating the photogenerated charges.[27] However, variations of steady-state PL intensity and average lifetime between BS-1 and BS-5 are small, indicating that, as for the obtained Bi_2S_3, bismuth vacancies had a positive effect but sulfur vacancies have no effect or a negative effect on suppressing the recombination rate.

To further disclose the photocatalytic bacterial inactivation mechanism, scavenger studies were conducted to determine the effects of those critical reactive species in NIR-driven photocatalytic bacterial inactivation. The scavengers employed in this study include Cr^{VI} (0.1 mM) for e^-, $Na_2C_2O_4$ (5 mM) for h^+, TEMPOL (1 mM; TEMPOL = 4-hydroxy-2,2,6,6-tetramethylpiperidinyloxy) for O_2^-, isopropanol (7.5 mM) for $^{\bullet}OH$, and Fe^{II}–EDTA (0.1 mM; EDTA = ethylenediaminetetraacetic acid) for H_2O_2. To ensure the maximum scavenging effect but no toxic or inactivation effects on the bacterial cells, the concentrations of each scavenger were optimized before conducting the scavenger study. Interestingly, after Cr^{VI} was added into system to capture e^-, the inactivation efficiency reduced significantly in comparison to that without scavenger addition, validating that the electrons are possible active species involved in the inactivation process (Figure 6 a). The addition of sodium oxalate to interact with h^+ also slightly inhibited photocatalytic inactivation, suggesting that h^+ also contributes to the bacterial inactivation process, although it is not the major reactive species. O_2^-, H_2O_2, and $^{\bullet}OH$ are well-known reactive oxygen species, of which the great oxidative potential would be too large for *E. coli* to endure.[28] With the addition of their corresponding scavengers, the inhibition effects were confirmed by a decrease in the inactivation efficiency, suggesting that O_2^-, H_2O_2, and $^{\bullet}OH$ are highly involved in the bacterial inactivation process. The involvement of O_2^- and $^{\bullet}OH$ was further verified by the ESR test (Figure 6 b, c). Both O_2^- and $^{\bullet}OH$ signals could be detected for the bismuth-deficient Bi_2S_3 within 4 min of NIR irradiation. In contrast, no O_2^- or $^{\bullet}OH$ signals could be detected under dark conditions, confirming their participation in the bacterial inactivation process. It seems that the contribution of O_2^- and H_2O_2 are slightly larger than that of $^{\bullet}OH$. On one hand, this is possibly because these reactive species are formed following the reduction pathway [Eqs. (2)–(5)]. On the other hand, the lifetimes of O_2^- ($t_{1/2} \approx 1$ µs) and H_2O_2 ($t_{1/2} \approx$ minutes to days)[29] are longer than that of $^{\bullet}OH$ ($t_{1/2} \approx 1$ ns).[30,31] Therefore, it would be easier for O_2^- and H_2O_2 than for $^{\bullet}OH$ to accumulate sufficiently to cause enough damage to the bacterial cells.

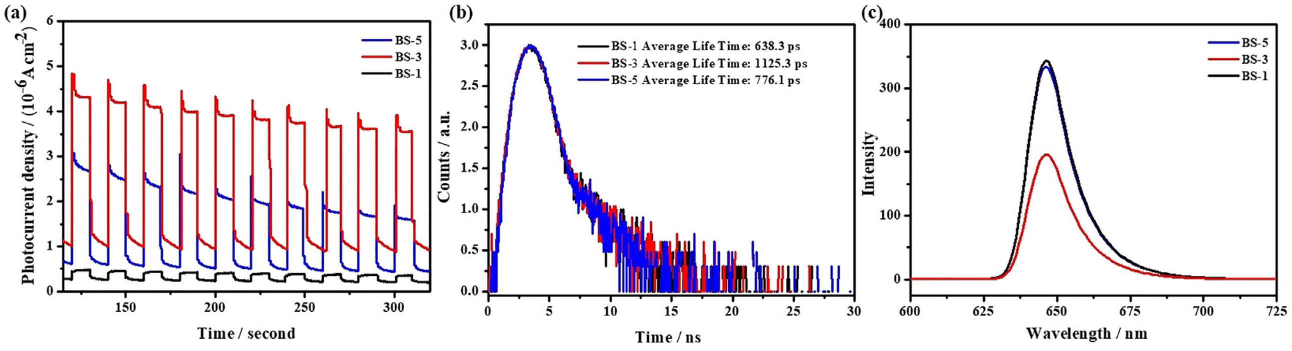

Figure 5. a) NIR irradiation-induced photocurrents, b) transient photoluminescence spectra, and c) steady state photoluminescence spectra for various Bi_2S_3 samples.

© 2019 Wiley-VCH Verlag GmbH & Co. KGaA, Weinheim

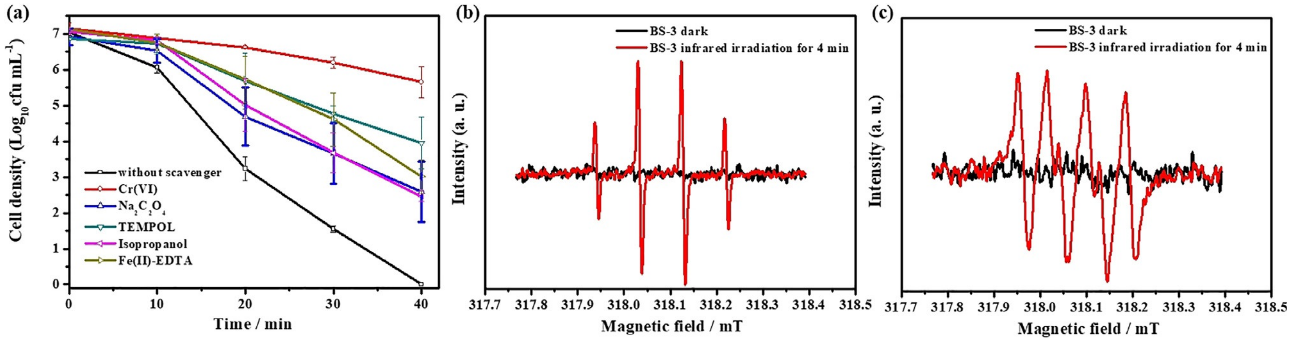

Figure 6. a) NIR-driven photocatalytic inactivation efficiency of *E. coli* by BS-3 with different scavengers. b, c) ESR spectra of hydroxyl radicals (b) and superoxide radicals (c) in the presence of BS-3 under NIR irradiation.

$$O_2 + e^- \rightarrow O_2^- \quad (2)$$

$$O_2^- + H^+ \rightarrow {}^{\bullet}HO_2 \quad (3)$$

$$ {}^{\bullet}HO_2 + H^+ + e^- \rightarrow H_2O_2 \quad (4)$$

$$H_2O_2 \rightarrow 2\,{}^{\bullet}OH \quad (5)$$

Based on the above analyses, the NIR-driven photocatalytic inactivation mechanism is proposed (Figure 7). As the spectral response of Bi_2S_3 extended to around 1000 nm, a NIR light source was applied. When Bi_2S_3 is irradiated by NIR, the incident light can be effectively utilized, owing to its prominent light absorption ability, which can excite the electron from the valence band to the conduction band. As discussed above, bismuth vacancies in Bi_2S_3 outperform sulfur vacancies in promoting the transfer of photogenerated electrons and suppressing electron–hole recombination. Therefore, the excited electron can efficiently transfer to the bismuth vacancy sites or bismuth vacancy-induced states. In the meantime, the bismuth vacancy sites also have an affinity for the adsorbed gaseous molecules.[11,32,33] As a result, the adsorbed molecular oxygen in bismuth vacancy sites is likely to be reduced to O_2^- by the trapped electrons at those bismuth vacancy sites if the potential of the excited electron is sufficient for the O_2/O_2^- transformation. The CBM was determined to be −0.76 V, which is thermodynamically favorable for the formation of O_2^- from O_2. Moreover, some of the formed O_2^- is further converted into H_2O_2 or ${}^{\bullet}OH$. These formed reactive species, as well as the photogenerated holes, then work together to attack *E. coli*, causing progressive damage to the bacteria cells.

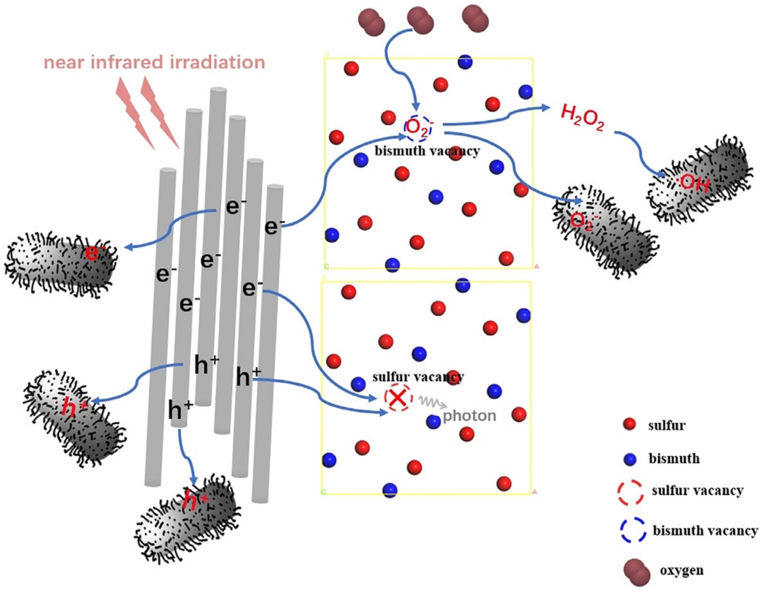

Figure 7. Proposed mechanism of NIR-driven photocatalytic inactivation of *E. coli* by bismuth-deficient Bi_2S_3.

Conclusions

Bi_2S_3 nanorods with different types of element vacancy were synthesized using a solvothermal method for which the treatment time was varied. Both sulfur and bismuth vacancies had been demonstrated to enhance the light absorption ability of Bi_2S_3. However, only bismuth vacancies led to increased charge densities of Bi_2S_3, extended the lifetime of the photogenerated charges by promoting the transfer of the electrons and suppressing the electron–hole recombination. Given these advantages, the bismuth-deficient Bi_2S_3 displayed an extraordinary NIR-driven photocatalytic bacterial inactivation efficiency, completely inactivating 7 log *E. coli* cells within 40 min under NIR irradiation and outperformed the sulfur-deficient Bi_2S_3. This study disclosed defect-type dependent photocatalytic behavior, providing new insights for designing highly efficient photocatalysts.

Experimental Section

Material synthesis

Defective Bi_2S_3 nanorods were fabricated using the solvothermal method. In a typical synthesis, bismuth nitrate pentahydrate (4 mmol) was dissolved in ethylene glycol (30 mL) to form solution A, and $Na_2S{\cdot}9H_2O$ (6 mmol) was dissolved in ethylene glycol (10 mL) through sonication to form solution B. Solution B was then added into solution A dropwise under continuous stirring. The mixed suspension was kept stirring for another 30 min, then transferred to the *p*-polyphenylenebased stainless steel autoclave for solvothermal treatment at 180 °C in an oven for 3 h. The sample was denoted as BS-3. When the treatment finished, the precipitates were filtered with a membrane filter (0.2 μm, Millipore), washed several times with deionized water and ethanol, and finally dried at 60 °C. Another two reference samples were prepared under similar conditions, but the duration time of the solvothermal treatment process were changed to 1 and 5 h and the samples were denoted as BS-1 and BS-5, respectively.

Material characterization

X-ray powder diffraction (XRD) patterns of the as-prepared samples were determined by a Rigaku Smartlab X-ray diffractometer with $Cu_{K\alpha}$ source irradiation ($\lambda = 1.5406$ Å). The microscopic features of the as-prepared sample were characterized by scanning electron microscopy (SEM) on a FEI Quanta 400 microscope, transmission electron microscopy (TEM) on a CM-120 microscope (Philips, 120 kV), and high resolution TEM as well as high angle annular dark field (HAADF) STEM on a Philips Tecnai F20 instrument. Energy dispersive X-ray spectroscopy (EDX) attached to the HRTEM was employed to analyze the elemental composition and distribution of the samples. Their specific surface areas and pore size distributions were evaluated by the Brunauer–Emmett–Teller (BET) and Barrett–Joyner–Halenda (BJH) methods. Electron paramagnetic resonance (EPR) spectroscopy of the samples was performed with a JES FA200 spectrometer (Jeol, Japan). X-ray photoelectron spectra (XPS) and valence band XPS spectra of the samples were recorded on ESCALAB 250Xi apparatus (Thermo Fisher Scientific) with $Al_{K\alpha}$ radiation (1486.6 eV) X-ray sources. The obtained spectra were calibrated with reference to the binding energy of C 1s (284.8 eV) and all peaks were well fitted by "XPSPEAK" analysis software. The light absorption abilities of the samples were determined by UV/Vis diffuse reflectance spectroscopy over a range of 200–2000 nm on a PerkinElmer Lambda 950 spectrometer. Room-temperature photoluminescence (PL) spectra of the samples were recorded by using a FP-6500 fluorescence spectrometer (Jasco, Japan) with an excitation wavelength of 365 nm. Time-resolved transient photoluminescence spectra of the samples were recorded (325 nm excitation) by a FLS980 Multifunction Steady State and Transient State Fluorescence Spectrometer (Edinburgh Instruments) at room temperature.

Photoelectrochemical measurements

Photoelectrochemical studies were conducted by using a three-electrode cell with a computer-controlled electrochemical workstation (CHI650E, Shanghai Chen Hua Instrument Company, China), among which platinum foil (1.0×1.0 cm^{-2}), a saturated potassium chloride–silver chloride electrode (Ag/AgCl), and the as-prepared sample were counter, reference, and working electrodes, respectively. The as-prepared samples were deposited on fluorine-doped tin oxide (FTO) glasses, which had been cleaned with absolute ethanol and deionized water. In a typical preparation, the as-prepared sample (5 mg), isopropanol (950 μL), and Nafion solution (~5 % in a mixture of lower aliphatic alcohols and water; 50 μL) were mixed by sonication to form a homogeneous catalyst colloid. The colloid (100 μL) was then deposited onto FTO glasses with areas of approximately 1 cm^2. The dried FTO glasses served as working electrodes and were immersed in 0.1 M Na_2SO_4 aqueous solution. A 300 W Xenon lamp equipped with a 700 nm cutoff filter was used as the irradiation source.

Photocatalytic inactivation of *Escherichia coli*

The Gram-negative bacterium *E. coli* was chosen as the model bacterium in this study as it is a nonpathogenic and well-studied model for laboratory experiments. *E. coli* was cultured in nutrient broth (50 mL, Lab M, Lancashire, UK) at 37 °C for 14 h in a shaking incubator. 1 mL of the cultured bacterial solution was washed twice with sterilized 0.9 % saline solution (1 mL of 0.9 g NaCl dissolved in 100 mL water). All glassware and equipment used in the photocatalytic reactions were washed, autoclaved, and dried. To start a photocatalytic disinfection experiment, the washed cell, the photocatalyst (20 mg), and sterilized saline solution (50 mL) were mixed in a beaker and the initial cell density was adjusted to 10^7 cfu mL^{-1}. A Xenon lamp coupled with a 700 nm long-pass filter was employed as the near-infrared (NIR) light source. During the photocatalytic disinfection process, aliquots of the mixture solution were collected at equal time intervals, and serially diluted with sterilized saline solution. Then the appropriately diluted sample (0.1 mL) was immediately spread on the nutrient agar (Lab M, Lancashire, U.K.) plates and incubated at 37 °C for 24 h to determine the survival rate of cells.

Acknowledgements

This research was financially supported by a research grant (GRF14100115) from the Research Grant Council, Hong Kong SAR Government, the National Natural Science Foundation of China (21706102 and 41425015), the Science and Technology Project of Guangdong Province, China (2017A050506049) and the Hong Kong Scholar Program (XJ2016034). P.K.W. was also supported by the CAS/SAFEA International Partnership Program for Creative Research Teams (2015HSC-UE004) of the Chinese Academy of Sciences, China. The authors would also like to acknowledge technical assistance from Dr. Zhuofeng Hu of the School of Chemistry, and Mr. Ho Yin Yip, Mr. Ho Shing Chan, Mr. Tsz Ho Tsang, and Ms. Kemeng Xiao of the School of Life Sciences at The Chinese University of Hong Kong.

Conflict of interest

The authors declare no conflict of interest.

Keywords: bismuth · defect engineering · electronic structure · photocatalysis · sulfides

[1] X. Q. Hao, J. Zhou, Z. W. Cui, Y. C. Wang, Y. Wang, Z. G. Zou, *Appl. Catal. B* **2018**, *229*, 41.
[2] T. Y. Ma, Y. Zheng, S. Dai, M. Jaroniec, S. Z. Qiao, *J. Mater. Chem. A* **2014**, *2*, 8676.
[3] M. Kong, Y. Z. Li, X. Chen, T. T. Tian, P. F. Fang, F. Zheng, X. J. Zhao, *J. Am. Chem. Soc.* **2011**, *133*, 16414.
[4] L. D. Li, J. Q. Yan, T. Wang, Z. J. Zhao, J. Zhang, J. L. Gong, N. J. Guan, *Nat. Commun.* **2015**, *6*, 5881.
[5] Y. B. Li, H. F. Wang, H. M. Zhang, P. R. Liu, Y. Wang, W. Q. Fang, H. G. Yang, Y. Li, H. J. Zhao, *Chem. Commun.* **2014**, *50*, 5569.
[6] Y. Zhang, F. Li, X. Zhang, T. Williams, C. D. Easton, A. M. Bond, J. Zhang, *J. Mater. Chem. A* **2018**, *6*, 4714.
[7] L. J. Liu, H. L. Zhao, J. M. Andino, Y. Li, *ACS Catal.* **2012**, *2*, 1817–1828.
[8] M. W. Shah, Y. Q. Zhu, X. Y. Fan, J. Zhao, Y. X. Li, S. Asim, C. Y. Wang, *Sci. Rep.* **2015**, *5*, 15804.
[9] Y. H. Lv, Y. F. Liu, Y. Y. Zhu, Y. F. Zhu, *J. Mater. Chem. A* **2014**, *2*, 1174.

© 2019 Wiley-VCH Verlag GmbH & Co. KGaA, Weinheim

[10] S. Y. Wang, X. Hai, X. Ding, K. Chang, Y. G. Xiang, X. G. Meng, Z. X. Yang, H. Chen, J. H. Ye, *Adv. Mater.* **2017**, *29*, 1701774.
[11] H. Li, J. Shang, Z. H. Ai, L. Z. Zhang, *J. Am. Chem. Soc.* **2015**, *137*, 6393.
[12] H. Li, J. G. Shi, K. Zhao, L. Z. Zhang, *Nanoscale* **2014**, *6*, 14168.
[13] J. Li, X. Wu, W. Pan, G. Zhang, H. Chen, *Angew. Chem. Int. Ed.* **2018**, *57*, 491; *Angew. Chem.* **2018**, *130*, 500.
[14] J. P. Wang, Z. Y. Wang, B. B. Huang, Y. D. Ma, Y. Y. Liu, X. Y. Qin, X. Y. Zhang, Y. Dai, *ACS Appl. Mater. Interfaces* **2012**, *4*, 4024.
[15] D. Li, S. H. Yu, H. L. Jiang, *Adv. Mater.* **2018**, *30*, 1707377.
[16] Y. H. Sang, Z. H. Zhao, M. W. Zhao, P. Hao, Y. H. Leng, H. Liu, *Adv. Mater.* **2015**, *27*, 363.
[17] J. Tian, Y. H. Sang, G. W. Yu, H. D. Jiang, X. N. Mu, H. Liu, *Adv. Mater.* **2013**, *25*, 5075.
[18] P. Yang, R. Wang, M. Zhou, X. Wang, *Angew. Chem. Int. Ed.* **2018**, *57*, 8674; *Angew. Chem.* **2018**, *130*, 8810.
[19] W. J. Wang, G. Y. Li, T. C. An, D. K. L. Chan, J. C. Yu, P. K. Wong, *Appl. Catal. B* **2018**, *238*, 126.
[20] X. Q. Hao, Y. C. Wang, J. Zhou, Z. W. Cui, Y. Wang, Z. G. Zou, *Appl. Catal. B* **2018**, *221*, 302.
[21] A. Y. Lu, X. L. Yang, C. C. Tseng, S. X. Min, S. H. Lin, C. L. Hsu, H. N. Li, H. C. Idriss, J. L. Kuo, K. W. Huang, L. J. Li, *Small* **2016**, *12*, 5530.
[22] H. Sheng, H. W. Ji, W. H. Ma, C. C. Chen, J. C. Zhao, *Angew. Chem. Int. Ed.* **2013**, *52*, 9686; *Angew. Chem.* **2013**, *125*, 9868.
[23] G. H. Moon, W. Kim, A. D. Bokare, N. E. Sung, W. Choi, *Energy Environ. Sci.* **2014**, *7*, 4023.
[24] L. Q. Yang, J. F. Huang, L. Shi, L. Y. Cao, Q. Yu, Y. N. Jie, J. Fei, H. B. Ouyang, J. H. Ye, *Appl. Catal. B* **2017**, *204*, 335.
[25] J. R. Ran, G. P. Gao, F. T. Li, T. Y. Ma, A. J. Du, S. Z. Qiao, *Nat. Commun.* **2017**, *8*, 13907.
[26] M. I. Saidaminov, J. Kim, A. Jain, R. Quintero-Bermudez, H. Tan, G. Long, F. Tan, A. Johnston, Y. Zhao, O. Voznyy, E. H. Sargent, *Nat. Energy* **2018**, *3*, 648.
[27] D. F. Xu, B. Cheng, W. K. Wang, C. J. Jiang, J. G. Yu, *Appl. Catal. B* **2018**, *231*, 368.
[28] D. Xia, Z. Shen, G. Huang, W. Wang, J. C. Yu, P. K. Wong, *Environ. Sci. Technol.* **2015**, *49*, 6264.
[29] H. W. Sun, G. Y. Li, X. Nie, H. X. Shi, P. K. Wong, H. J. Zhao, T. C. An, *Environ. Sci. Technol.* **2014**, *48*, 9412.
[30] Y. Nosaka, A. Y. Nosaka, *Chem. Rev.* **2017**, *117*, 11302.
[31] B. S. Winkler, M. E. Boulton, J. D. Gottsch, P. Sternberg, *Mol. Vision* **1999**, *5*, 24.
[32] J. Lee, D. C. Sorescu, X. Deng, *J. Am. Chem. Soc.* **2011**, *133*, 10066.
[33] M. Setvin, U. Aschauer, P. Scheiber, Y. F. Li, W. Hou, M. Schmid, A. Selloni, U. Diebold, *Science* **2013**, *341*, 988.

Manuscript received: October 22, 2018
Revised manuscript received: November 20, 2018
Accepted manuscript online: November 29, 2018
Version of record online: January 22, 2019

© 2019 Wiley-VCH Verlag GmbH & Co. KGaA, Weinheim